Analytical and Bioanalytical Chemistry (2018) 410:6733–6749
https://doi.org/10.1007/s00216-018-1295-0

PAPER IN FOREFRONT

Longitudinal investigation of the metabolome of 3D aggregating brain cell cultures at different maturation stages by ^{1}H HR-MAS NMR

Gaëlle Diserens[1] · Martina Vermathen[2] · Marie-Gabrielle Zurich[3,4] · Peter Vermathen[1]

Received: 2 May 2018 / Revised: 25 June 2018 / Accepted: 26 July 2018 / Published online: 10 August 2018

Abstract

The aim of the present study was to establish the developmental profile of metabolic changes of 3D aggregating brain cell cultures by ^{1}H high-resolution magic angle spinning (HR-MAS) NMR spectroscopy. The histotypic 3D brain aggregate, containing all brain cell types, is an excellent model for mechanistic studies including OMICS analysis; however, their metabolic profile has not been yet fully investigated. Chemometric analysis revealed a clear separation of samples from the different maturation time points. Metabolite concentration evolutions could be followed and revealed strong and various metabolic alterations. The strong metabolite evolution emphasizes the brain modeling complexity during maturation, possibly reflecting physiological processes of brain tissue development. The small observed intra- and inter-experimental variabilities show the robustness of the combination of ^{1}H-HR-MAS NMR and 3D brain aggregates, making it useful to investigate mechanisms of toxicity that will ultimately contribute to improve predictive neurotoxicology.

Keywords High-resolution magic angle spinning · Nuclear magnetic resonance · 3D brain cell cultures · Brain aggregates · Chemometrics

Introduction

The central nervous system (CNS) is one of the most complex organ systems in terms of both structure and function; in addition, the lack of regeneration after severe damage renders the nervous system unique and particularly vulnerable to toxic insult. Neurotoxic effects in human have been shown for different compounds with the largest groups being metals, organic solvents, and pesticides [1]. In addition, the increasing onset of neuronal disorders and neurodegenerative diseases, linked to the aging of the population, represents a clear demand for CNS active drugs for which safety has to be assessed in the early phase of development. However, about 4% of the prescription drugs withdrawn from the market were based on neurotoxic effects [2, 3].

Guidelines on neurotoxicity testing prescribe in vivo animal tests to determine developmental and adult neurotoxic effects, both after acute and chronic exposure [4–7]. Since these tests are expensive, time-consuming, and give rise to ethical issues, alternatives are needed. Neurotoxicity is the outcome of complex interactions of xenobiotics at the molecular, cellular, and tissue level of the central and/or peripheral nervous system triggering an adverse effect. An adverse effect can be caused by changes of neuronal and/or glial chemistry, structure, and/or function. Therefore, any in vitro testing strategy for neurotoxicity evaluation has to be based on the combination of relevant in vitro models that possess the necessary molecular mechanisms and pathways that can be evaluated in a quantitative manner by sensitive, neuronal, and glia-specific endpoints [5, 8]. The 3D rat brain aggregate model is

Marie-Gabrielle Zurich and Peter Vermathen contributed equally to this work.

Electronic supplementary material The online version of this article (https://doi.org/10.1007/s00216-018-1295-0) contains supplementary material, which is available to authorized users.

✉ Peter Vermathen
peter.vermathen@insel.ch

[1] Departments of BioMedical Research and Radiology, University of Bern, Erlachstrasse 9a, 3012 Bern, Switzerland

[2] Department of Chemistry and Biochemistry, University of Bern, Freiestrasse 3, 3012 Bern, Switzerland

[3] Department of Physiology, University of Lausanne, Rue du Bugnon 7, 1005 Lausanne, Switzerland

[4] Swiss Center for Applied Human Toxicology (SCAHT), Basel, Switzerland

composed of all brain cell types, neurons, astrocytes, oligodendrocytes, and microglial cells, and presents a very high level of cell organization, similar to in vivo brain tissue cyto-architecture and function as indicated by the final ratio of neurons to glial cells, the formation of an organotypic cyto-architecture, the correct timing, and extent of developmental events such as cell proliferation, synaptogenesis, myelination, and the elaboration of neuronal networks [9]. This model is an excellent tool for mechanistic studies, including OMICS analysis [10]. It has been extensively used for neurotoxicological investigations and was shown to be a highly sensitive and reliable in vitro model to detect CNS-specific toxicity [11, 12]. The long-term stability makes the 3D model applicable for investigations of both acute and repeated exposure to chemicals or drugs. This model has also proven valuable to probe maturation-dependent neurotoxicity [13]. Furthermore, the aggregating cells have also potential to investigate neurological disorders or brain infections including Zika virus-linked brain infections [14]. Detection of metabolic alterations as potential biomarkers is well suited to monitor neurotoxicity. However, as a precondition for neurotoxicological testing, the developmental metabolic profile of maturating 3D cell cultures, its stability, and reproducibility need to be established. Furthermore, the determination of developmental metabolic changes with maturation may help to select the best window of vulnerability for exposure of the cells to potential neurotoxins and may additionally also provide insight into early brain cell development.

Metabolic changes of the developing brain have been investigated non-invasively by in vivo MR spectroscopy in animal models and also in humans [15–21]. For ex vivo applications, nuclear magnetic resonance (NMR) spectroscopy has been established in recent years, besides mass spectrometry, as important tool for metabolic profiling in pathology and toxicology [22, 23]. Besides the potential of NMR for biofluids, High-Resolution Magic Angle Spinning NMR (HR-MAS NMR) offers the possibility to profile the metabolic pattern of cells and biopsies, without the need of tissue/cell extraction or separation steps, and to determine metabolite concentrations close to living conditions, because of minimal intervention into tissue biochemistry. Fast spinning around an axis inclined at an angle of 54.7° with respect to the axis of the external magnetic field can average orientation dependent effects close to zero, thereby significantly reducing the linewidth and increasing both the spectral resolution and sensitivity [24]. While metabolic profiling of cultured 2D cells employing HR-MAS NMR has been applied in several studies [25–27], 3D aggregating cell culture models or 3D tissue slice cultures have been investigated only rarely by HR-MAS NMR [28–30]. Close similarities between cells in spheroids and intact tissue have been emphasized in several NMR studies performed on 3D cell cultures without spinning [31–34]. 3D brain cell culture extracts were recently measured by NMR [10] to investigate the metabolite changes after toxin exposure to drugs. Extracellular metabolic changes of rat brain cell aggregates have been investigated during cell growth; glucose, lactate, and ammonia were determined as well as amino acids by HPLC [35].

Metabolite changes during chick embryo brain maturation from incubation days 10 to 20 and postnatal day 1 have been investigated by ^{1}H HR-MAS NMR to better understand the embryonic brain development [36]. However, despite the described potential of 3D cell cultures for evaluation of growth kinetics including cell proliferation and myelination, no study has investigated metabolic changes during maturation by HR-MAS or in neurotoxicological investigations.

The overall aim of this study was therefore to metabolically characterize cellular growth by employing ^{1}H HR-MAS NMR as minimally interfering analytical method in aggregating 3D brain cell cultures at different maturation stages. It was intended to establish a developmental profile of metabolic changes to set up the basis for subsequent toxicological studies. The specific aims were to determine the metabolite stability and variability between different cell culture batches and to examine metabolic changes during cell maturation.

Materials and methods

Aggregating brain cell cultures

Ethical approval was obtained (authorization number VD3128 delivered by the local veterinary office). 3D aggregating brain cell cultures (AGGR) derived from embryonic (16-day) rat brain were prepared as previously described [37]. Briefly, the dissected brain tissue was dissociated mechanically using nylon sieves of 200- and 115-μm pores. The dissociated and washed cells were re-suspended in serum-free modified DMEM. Aliquots of the cell suspension were transferred to culture flasks and maintained under constant gyratory agitation at 37 °C in an atmosphere of 10% CO_2 and 90% humidified air. Media were replenished by replacing 5 mL of medium (of a total of 8 mL) with 5 mL of fresh medium at intervals of 3 days until day 14 of in vitro culture and at intervals of 2 days thereafter.

Forty-two AGGR samples were collected at five different time points, at day in vitro (DIV) 7, 14, 21, 28, and 35. The samples originated from four different brain batches (biological replicates) and included up to three technical replicates, which were created from pooled and redistributed free-floating aggregates. Nine AGGR samples were harvested at each time point, with the exception of DIV 35 (six AGGR samples). Table S1 in the Electronic Supplementary Material (ESM) summarizes the number of samples measured at each of the five DIV for the four different brain batches. Samples were washed two times with ice-cold phosphate-buffered

saline solution (PBS). The PBS was removed and the samples immediately transferred to dry ice and stored at − 80 °C until HR-MAS NMR measurement. Sample replicates for DIV 7, 14, and 21 were obtained from a "whole flask", i.e., the content of the flask was not split after the distribution of the single-cell suspension at culture start. Sample replicates at DIVs 28 and 35 correspond to the half of a whole flask. Each replicate culture contained an average of 150–200 aggregates.

Additionally, the supernatants of cell media were collected from the same batches and DIVs plus additional samples from DIV 26. Media were collected by pipetting 1.2 mL of medium twice into an Eppendorf vial after letting the aggregates settle down. The media were centrifuged at 300×*g* for 5 min at 4 °C and 1 mL of each sample was stored at − 80 °C. Overall, 84 supernatants were collected (15 samples at each of DIV 7, 14, 21, and 35; 11 samples at DIV 26; 13 samples at DIV 28).

NMR spectroscopy

Sample preparation Each of the 42 AGGR samples was thawed at room temperature and transferred with added 15 μL of D_2O-based PBS (pH 7, 50 mM) into a 4-mm zirconia MAS rotor using a 50-μL insert. The samples were measured in random order. The preparation time from the beginning of thawing until start of the NMR experiments (including rotor filling and NMR optimization with shimming, water suppression, etc.) was kept short and as good as possible identical for all samples. The time from taking the sample out of freezer until start of the NMR acquisition took 24.9 ± 3.7 min.

Acquisition ^{1}H HR-MAS NMR experiments were performed on a Bruker Avance II spectrometer (Bruker BioSpin) operating at a resonance frequency of 500.13 MHz for ^{1}H, using a 4-mm HR-MAS dual inverse ^{1}H/^{13}C probe equipped with a magic angle gradient.

For the cell aggregates, spectra were acquired at a spinning speed of 3 kHz. A 1D *PROJECT* sequence [38] with water presaturation was measured at an actual temperature of 284 K, with 512 transients, a spectral width of 6010 Hz, a data size of 32 K points, an acquisition time of 2.73 s, a relaxation delay of 4 s, an echo time (TE) of 400 ms, and a rotor-synchronized interpulse delay of 1.33 ms. Preliminary measurements with different TEs showed that signal intensities of small metabolites were still sufficiently strong at a TE of 400 ms due to long relaxation times (results not shown). The long echo time allows suppressing the lipids and virtually eliminates overlap of small metabolites with lipid peaks, thus simplifying spectral analysis. A 1D NOESY sequence ("*noesypr1d*" from the Bruker pulse program library) was used for investigating primarily lipids, applying 128 transients, a spectral width of 7002.8 Hz, a data size of 32 K points, an acquisition time of 2.34 s, and a relaxation delay of 4 s. The noesy mixing time was 10 ms. The 90° pulse length and water presaturation were optimized for each measurement. For selected samples, phase-sensitive 2D-^{1}H^{1}H-TOCSY spectra using the DIPSI sequence ("*dipsi2phpr*" from the Bruker pulse program library) with water presaturation were recorded to help spectral assignment.

For the supernatants, only a 1D NOESY sequence with water presaturation ("*noesygppr1d*") was applied because lipids and broad underlying resonances were absent. The measurements were performed at 298 K with 128 transients, a spectral width of 6009.6 Hz, a data size of 64 K points, an acquisition time of 5.45 s, and a relaxation delay of 6 s.

Data processing

Bruker Topspin™ software (v. 3.5) was used for processing the spectra. For all 1D spectra (PROJECT and NOESY spectra), the co-added free induction decays (FIDs) were exponentially weighted with a line broadening factor of 0.5 Hz, Fourier-transformed, phased, and baseline corrected (linear order) and the frequency was calibrated to the lactate -CH_3- resonance (doublet) at 1.32 ppm.

Analysis

Bucketing For cell aggregates, 303 spectral regions ("buckets") of variable size according to the peak width were manually selected between 0.8 and 10.0 ppm of the PROJECT spectra and integrated, leaving out spectral regions comprising only noise. To account for differences in cell numbers per sample, the spectra were normalized using probabilistic quotient normalization (PQN) [39]. Unfortunately, an absolute quantification was not possible because the exact weight of the cell culture samples needs to be known. Although the sample weights were measured, varying amounts of accompanying PBS rendered this estimation very imprecise. For supernatants, 244 buckets of variable size depending on the peak width were selected accordingly between 0.8 and 9.0 ppm.

Signal annotation After assigning the buckets to metabolites (see "Results and discussion" section), a single value for each metabolite was determined by merging the different buckets belonging to the same metabolite, considering in addition the impact of overlapping peaks (leaving them out when possible).

Chemometric analysis In order to determine which metabolites and buckets were subject to strongest developmental changes, chemometric analysis was performed. For chemometric analysis, the buckets were mean centered and scaled with Pareto scaling. Principal Component Analysis (PCA), a non-supervised method, and orthogonal Partial Least Squares (oPLS) analysis using the developmental day as continuous

observable variable as prior knowledge were performed with PLS_Toolbox (Eigenvector Research, Inc). PCA and oPLS were performed twice, first employing only the assigned metabolites and secondly employing all buckets (for an unbiased analysis considering also unassigned and strongly overlapping peaks). The PLS models were subsequently cross-validated and subjected to permutation testing (50 iterations).

Individual analysis Additionally, the content evolution over different developmental stages was analyzed individually for a number of metabolites. Temporal metabolic changes were fitted with Matlab (R2014b, The MathWorks Inc.) assuming zero-, first-, or second-order kinetics.

Analysis of variation In order to investigate the metabolic stability and estimate repeatability between and within the different brain batches, coefficients of variation were calculated for the cell aggregates. The 303 normalized buckets of the PROJECT spectra were used for the calculation of the coefficient of variation *within* technical replicates (CVw) and *between* biological replicates, i.e., between the different brain batches (CVb) for each of the DIV (see ESM Table S1). Buckets with intensities below 20% of the mean intensity were excluded from the analysis, leaving 162 buckets for the calculation of the CVs.

Lipids Lipid peaks of the NOESY spectra were manually integrated and normalized using the PQN factors obtained from the corresponding PROJECT spectra of the same aggregates. This normalization was selected instead of normalization to the total intensity or PQN factors of the NOESY spectra themselves in order to prevent spurious normalization in case of a total lipid change during maturation.

Results and discussion

^{1}H HR-MAS NMR spectra of brain aggregates

The spectral assignment of AGGR brain cell cultures is shown in Fig. 1 on an averaged PROJECT spectrum from samples collected at DIV 7. The lipids are mostly suppressed due to the T2 filter. More than 40 metabolites were assigned based on additionally performed 2D-TOCSY measurements, own reference spectra, the HMDB database [40], and literature references [25]. Still, several peaks remain unassigned and require further investigations. All assigned resonances are also listed in Table 1 together with cross-peaks from the 2D-TOCSY spectra.

Many metabolites that were assigned here in spectra from rat brain cell aggregates have also been determined in the rodent and human brain by in vivo NMR spectroscopy [41–43]. Similarly, an ex vivo high-resolution ^{1}H NMR study on rat brain extracts quantified 27 different metabolites (plus ethanol and methanol as contaminants) [44], most of which were also detected in the current study in brain aggregates. However, few metabolites that have been measured by NMR in the brain could not be unambiguously assigned, including ethanolamine, scyllo-inositol, or pyruvate, and vice versa several metabolites that were detected here in the rat brain cultures have been described only rarely in in vivo or ex vivo NMR measurements of brain tissue. Proline (Pro) for instance was found at high concentrations at a very early developmental stage, although it has not been reported in vivo by NMR [41, 42, 45] and is present only at low concentrations in brain [46]. It has to be noted that the first day of culture (DIV 1) corresponds to gestational day 17, i.e., roughly 1 week before birth, and although the cells reach a very high level of maturation at DIV 35, they mimic more juvenile than adult brains. Thus, our detection of Pro is not contradictory with its low levels in brain tissue, since the level of Pro strongly decreases with time in culture. Interestingly, hypotaurine (Hypotau), a precursor of taurine (Tau), was clearly detected in the AGGR brain cell cultures, as confirmed by cross-peaks on the 2D-TOCSY spectra, and increased over the time in culture, while the Tau content decreased after an initial strong increase. Hypotau is mainly built in astrocytes after conversion of cysteine to cysteine-sulfinic acid followed by a decarboxylation and is then converted to taurine in astrocytes and neurons [47]. Notably, the evolution of Tau concentration, showing a peak at DIV15 which corresponds to the first week after birth, follows the same pattern as in the human brain where the concentration of Tau is high at the time of birth and decreases with age [41, 48].

While very low at DIV 7 and strongly overlapping with Pro resonances, a resonance due to a *N*-acetyl moiety arises at 2.01 ppm at later developmental stages (see Fig. 2), which most likely originates from *N*-acetylaspartate (NAA), the second highest amino acid in the brain. However, further confirmation of the unambiguous NAA assignment is warranted, because the corresponding resonances at ~2.7 and ~4.4 ppm were present, but the expected cross-peaks were hardly detectable in the TOCSY spectra.

Coefficients of variation

The coefficients of variation (CVs) were calculated to investigate the variability within the same brain batches (i.e., originating from the same pool of rat embryos) and between brain batches (i.e., originating from different pools of rat embryos). This information is essential for planning potential later investigations after a challenge, e.g., for toxicological studies. The variances are most likely mainly due to differences in metabolite concentrations; however, a small contribution may also derive from differences in relaxation times due to the relatively long echo time of 400 ms used in the PROJECT sequence.

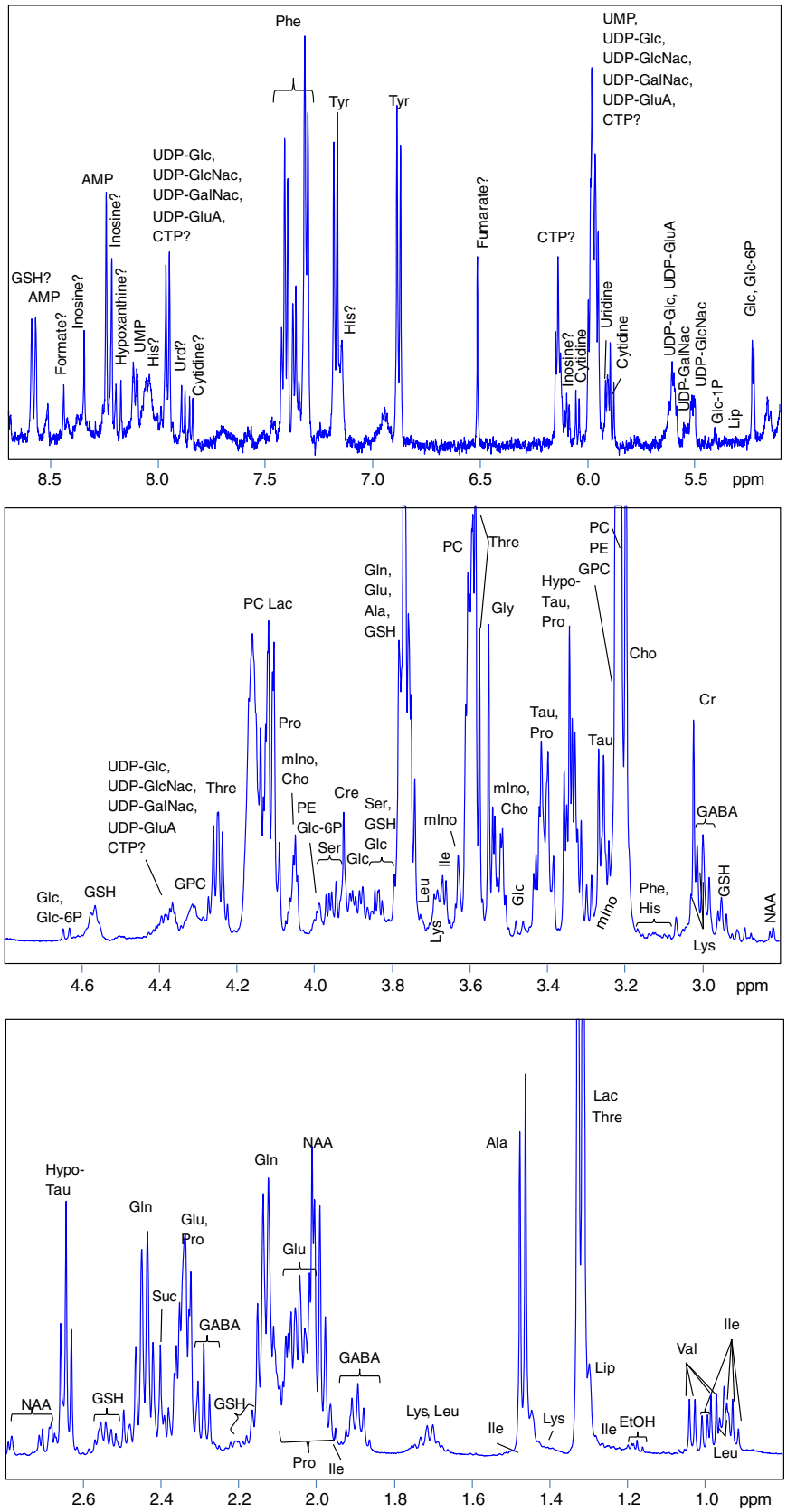

Fig. 1 Averaged ^{1}H HR-MAS NMR spectrum of 3D brain cell cultures collected at DIV 7, with principal metabolite assignment. Metabolites labeled with "question mark" require further confirmation

The average CVs between and within batches were relatively low and were significantly smaller within batches (7.6%) compared to between batches (10.0%) for the mean of the different DIV as well as for each of the five investigated

Table 1 Signal assignment of protons from AGGR cells

Peak	Chemical Shift [ppm]	Compound	TOCSY [ppm]	Group
1	0.929 (t)	Isoleucine (Ile)	1.00, 1.24, 1.45, 1.97	δ-CH_3
2	0.95 (d)	Leucine (Leu)	1.71, 3.74	δ-CH_3
3	0.98 (d)	Valine (Val)	1.03, 2.27, 3.62	γ-CH_3
4	1.002 (d)	Isoleucine (Ile)	0.93, 1.24, 1.45, 1.99, 3.67	β′-CH_3
5	1.034 (d)	Valine (Val)	0.98, 2.27, 3.62	γ-CH_3
6	1.195 (t)	Ethanol (EtOH)	3.66	-CH_3
7	1.242 (m)	Isoleucine (Ile)	0.93, 1.01, 1.45, 1.97	γ-CH_2
8	1.297 (br)	Lipid (Lip)		$(-CH_2)_n$
9	1.32 (d)	Lactate (Lac)	4.116	β-CH_3
10	1.32 (d)	Threonine (Thr)	3.58, 4.25	γ-CH_3
11	1.45	Lysine (Lys)	1.71, 1.88, 3.015	γ-CH_2
12	1.447 (m)	Isoleucine (Ile)	0.93, 1.01, 1.24, 1.98	γ-CH_2
13	1.47 (d)	Alanine (Ala)	3.77	β-CH_3
14	1.708 (m)	Leucine (Leu)	0.95, 3.74	γ-CH, β-CH_2
15	1.71 (m)	Lysine (Lys)	1.45, 1.88, 3.015	δ-CH_2
16	1.88 (m)	Lysine (Lys)	1.45, 1.71, 3.015	β-CH_2
17	1.892 (m)	4-Aminobutyric acid (GABA)	2.29, 3.00	β-CH_2
18	1.966 (m)	Isoleucine (Ile)	0.93, 1.00, 1.24, 1.45	β-CH
19	1.99 (m)	Proline (Pro)	2.34, 3.33, 3.41, 4.13	γ-CH_2
20	2.063 (m)	Proline (Pro)	2.34, 3.33, 3.41, 4.13	γ-CH_2
21	2.055 (m)	Glutamate (Glu)	2.35, 3.76	β-CH_2
22	2.01 (s)	*N*-acetyl-aspartate (NAA)		-CH_3(Acetyl)
23	2.15 (m)	Glutamine (Gln)	2.45, 3.79	β-CH_2
24	2.157 (m)	Glutathione (GSH)	2.55, 3.78	β-CH_2(Glu)
25	2.288 (t)	4-Aminobutyric acid (GABA)	1.89, 3.00	α-CH_2
26	2.34 (m)	Proline (Pro)	1.99, 3.33, 3.41, 4.13	β-CH_2
27	2.35 (m)	Glutamate (Glu)	2.06, 3.76	γ -CH_2
28	2.407 (s)	Succinate (Suc)	–	α-CH_2
29	2.45 (m)	Glutamine (Gln)	2.15, 3.79	γ-CH_2
30	2.546 (m)	Glutathione (GSH)	2.16, 3.78	γ-CH_2(Glu)
31	2.642 (t)	Hypotaurine (Hypotau)	3.343	α-CH_2
32	2.69 (dd)	*N*-acetyl-aspartate (NAA)		β-CH_2
33	2.8 (dd)	*N*-acetyl-aspartate (NAA)		β-CH_2
34	2.956 (m)	Glutathione (GSH)	4.57, 8.58	β-CH_2(Cys)
35	2.998 (t)	4-Aminobutyric acid (GABA)	1.89, 2.29	γ-CH_2
36	3.015 (t)	Lysine (Lys)	1.45, 1.71, 1.88	ε-CH_2
37	3.023	Creatine (Cre)		-CH_3
38	3.11 (dd)	Phenylalanine (Phe)	3.28, 3.98	β-CH_2
39	3.14 (dd)	Histidine (His)	3.23, 3.99	β-CH_2
40	3.198 (s)	Choline (Cho)		-$N^+(CH_3)_3$
41	3.215 (s)	Phosphocholine (PC)		-$N^+(CH_3)_3$
42	3.217 (t)	Phosphoethanolamine (PE)	3.977	-CH_2
43	3.226 (s)	Glycerophosphocholine (GPC)		-$N^+(CH_3)_3$
44	3.23 (dd)	Histidine (His)	3.14, 3.99	β-CH_2
45[a]	3.24 (dd)	Glucose (Glc)	3.40, 3.48, 4.65	-CH
46	3.27 (t)	Myo-inositol (mIno)	3.53, 3.61, 4.05	-CH
47	3.255 (t)	Taurine (Tau)	3.42	α-CH_2
48	3.28 (dd)	Phenylalanine (Phe)	3.11, 3.98	β-CH_2
49	3.33 (m)	Proline (Pro)	1.99, 2,34, 3.41, 4.13	-CH_2

Table 1 (continued)

Peak	Chemical Shift [ppm]	Compound	TOCSY [ppm]	Group
50	3.343 (t)	Hypotaurine (Hypotau)	2.642	β-CH_2
51[a]	3.38-3.55	Glucose (Glc)	Multiple	-CH
52	3.41 (m)	Proline (Pro)	1.99, 2,34, 3.33, 4.13	-CH_2
53	3.417 (t)	Taurine (Tau)	3.26	β-CH_2
54	3.53 (dd)	Myo-inositol (mIno)	3.27, 3.61, 4.05	-CH
55	3.52 (m)	Choline (Cho)	4.06	-CH_2
56	3.552 (s)	Glycine (Gly)	–	α-CH_2
57	3.58 (d)	Threonine (Thr)	1.32, 4.25	α-CH
58	3.595 (m)	Phosphocholine (PC)	4.16	-CH_2
59	3.61 (t)	Myo-inositol (mIno)	3.27, 3.53, 4.05	-CH
60	3.665 (d)	Isoleucine (Ile)	1.01	α -CH
61	3.68 (t)	Lysine (Lys)		α -CH
62	3.68 (m)	Glycerophosphocholine (GPC)	4.32	-CH_2
63[a]	3.69-3.93	Glucose (Glc)	Multiple	-CH, -CH_2
64	3.727 (m)	Leucine (Leu)	0.95, 1.71	α -CH
65	3.76 (m)	Glutamate (Glu)	2.06, 2.35	α-CH
66	3.79 (m)	Glutamine (Gln)	2.15, 2.45	α-CH
67	3.77 (q)	Alanine (Ala)	1.47	α-CH
68	3.78 (t)	Glutathione (GSH)	2.16, 2.55	α-CH(Glu)
69	3.835 (m)	Serine (Ser)	3.96	α-CH
70	3.84 (d)	Glutathione (GSH)		-CH_2(Gly)
71	3.926	Creatine (Cre)		-CH_2
72	3.96 (m)	Serine (Ser)	3.84	β-CH_2
73	3.977 (m)	Phosphoethanolamine (PE)	3.217	-CH_2
74	3.98 (dd)	Phenylalanine (Phe)	3.11, 3.28	α -CH
75	3.99 (dd)	Histidine (His)	3.14, 3.23	α-CH_2
76	3.993 (dd)	Glucose-6-phosphate (Glc-6P)	3.51	-CH
77	4.05 (t)	Myo-inositol (mIno)	3.27, 3.53, 3.61	-CH
78	4.06 (m)	Choline (Cho)	3.52	-CH_2
79	4.116 (q)	Lactate (Lac)	1.32	α-CH
80	4.126 (m)	Proline (Pro)	1.99, 2,34, 3.33, 3.41	α-CH
81	4.16 (m)	Phosphocholine (PC)	3.60	-CH_2
82	4.25 (m)	Threonine (Thr)	1.32, 3.58	β-CH_2
83	4.318 (m)	Glycerophosphocholine (GPC)	3.68	-CH_2
84	4.40 (m)	UDP-Glc, UDP-GlcNac, UDP-GalNac, UDP-GluA	5.966	-CH (Rib)
85	4.38 (m)	*N*-acetyl-aspartate (NAA)		α-CH
86	4.57 (m)	Glutathione (GSH)	2.96, 8.58	-CH
87	4.646 (d)	Glucose (Glc), glucose-6-phosphate (Glc-6P)	3.25, 3.38, 3.42, 3.47, 3.51	-CH-1
88	5.23 (d)	Glucose (Glc), glucose-6-phosphate (Glc-6P)	3.41, 3.54, 3.71	-CH-1
89	5.31 (br)	Lipid		-CH=CH
90	5.445 (dd)	Glucose-1-phosphate (Glc-1P)		-CH-1 (Glc)
91	5.515 (dd)	UDP-*N*-acetyl-glucosamine (UDP-GlcNac)		-CH-1 (Glc)
92	5.546 (dd)	UDP-*N*-acetyl-galactosamine (UDP-GalNac)		-CH-1 (Gal)
93	5.611 (dd)	UDP-glucuronic acid (UDP-GluA)		-CH-1(GlcA)
94	5.602	UDP-Glucose (UDP-Glc)		-CH-1 (Glc)
95	5.899 (d)	Cytidine	4.21, 4.31	-CH
96	5.906 (m)	Uridine (Urd)	7.88	-CH
97	5.966 (m)	UMP, UDP-Glc, UDP-GlcNac, UDP-GalNac, UDP-GluA	8.113 (UMP), 7.96, 4.40	-CH
98	6.045 (d)	Cytidine	7.85	-CH

Table 1 (continued)

Peak	Chemical Shift [ppm]	Compound	TOCSY [ppm]	Group
99	6.089 (d)	Inosine?	4.44, 4.78	-CH (ribose)
100	6.513 (s)	Fumarate	–	-CH
101	6.88 (d)	Tyrosine (Tyr)	7.18	-CH
102	7.15 (s)	Histidine (His)		-CH (imidazole)
103	7.175 (d)	Tyrosine (Tyr)	6.88	-CH
104	7.31 (d)	Phenylalanine (Phe)	7.37, 7.41	-CH
105	7.366 (m)	Phenylalanine (Phe)	7.31, 7.41	-CH
106	7.413 (m)	Phenylalanine (Phe)	7.31, 7.37	-CH
107	7.848 (d)	Cytidine	6.05	-CH
108	7.88 (d)	Uridine (Urd)	5.906	-CH
109	7.96 (d)	UDP-Glc, UDP-GlcNac, UDP-GalNac, UDP-GluA	5.97	
110	8.04 (s)	Histidine (His)		-CH (imidazole)
111	8.113 (d)	UMP	5.966	-CH (uracil)
112	8.187 (d)	*N*-acetyl-aspartate (NAA)		-NH
113	8.193 (s)	Hypoxanthine	–	-CH
114	8.214 (s)	Hypoxanthine	–	-CH
115	8.219 (s)	Inosine	–	-CH (hypoxanthine)
116	8.222 (s)	AMP		
117	8.348 (s)	Inosine	–	-CH (hypoxanthine)
118	8.453 (s)	Formate	–	-CH
119	8.58	Glutathione (GSH), AMP	2.96, 4.57	-NH (Cys)

[a] Primarily detectable at later developmental stages

DIV (see Table 2). This suggests generally a greater similarity in samples originating from the same pool of rat embryos, compared to samples originating from different rat embryos. Although higher than the CVw, the CVb are also small, with a mean variability of 10.0% (between 7.8 and 12.2% depending on the maturation day) and the difference between CVb and CVw appears to become smaller at later stages. This result reflects the overall stability of the development of the AGGR, independently of which pool of rat embryos was used for their generations.

Metabolic changes over time

Figure 2 shows mean spectra of AGGR brain cell cultures collected at DIVs 7, 14, 21, 28, and 35, for the spectral regions between 1.4 and 4 ppm and between 5 and 8.8 ppm. Some prominent temporal peak modifications are highlighted. Already the visual inspection reveals that the metabolite content strongly evolves during cell culture maturation for a number of different metabolites.

Metabolic changes over time were assessed in two different ways, first by chemometric methods assessing all resonances and metabolites simultaneously and secondly by individual metabolite kinetic analysis.

Chemometric analysis

Chemometric analysis performed on the assigned metabolites of the brain aggregates revealed a clear separation of the different developmental time points (DIVs 7, 14, 21, 28, 35), both using unsupervised PCA (Fig. 3a, with a slight overlap of confidence intervals for DIVs 14 and 21 and DIVs 28 and 35) and supervised oPLS (Fig. 3b). The separation was strongest between days 7 and 14, i.e., main metabolic changes appeared at an early developmental stage. Similar to the PCA, the oPLS analysis with the time in culture as continuous observable variable (*y*-matrix) leads to a complete and significant separation of the samples collected at the different development stages (Fig. 3b) ($Q^2 = 0.98$, Permutation test: $p < 0.001$). A continuous path between the different maturation stages can be seen, while samples from same developmental stages cluster closely. The loading plot of the latent variables LV1 vs. LV2 suggests, e.g., phosphocholine (PC), Hypotau, taurine (Tau), choline (Cho), and creatine (Cre) as main discriminating, i.e., most strongly changing metabolites (Fig. 3c). It should be noted however that the stronger impact of these metabolites is partly due to their higher concentration and that other metabolites also go through strong relative changes over time. In order to additionally determine the impact of unassigned and strongly overlapping peaks, the PCA and oPLS

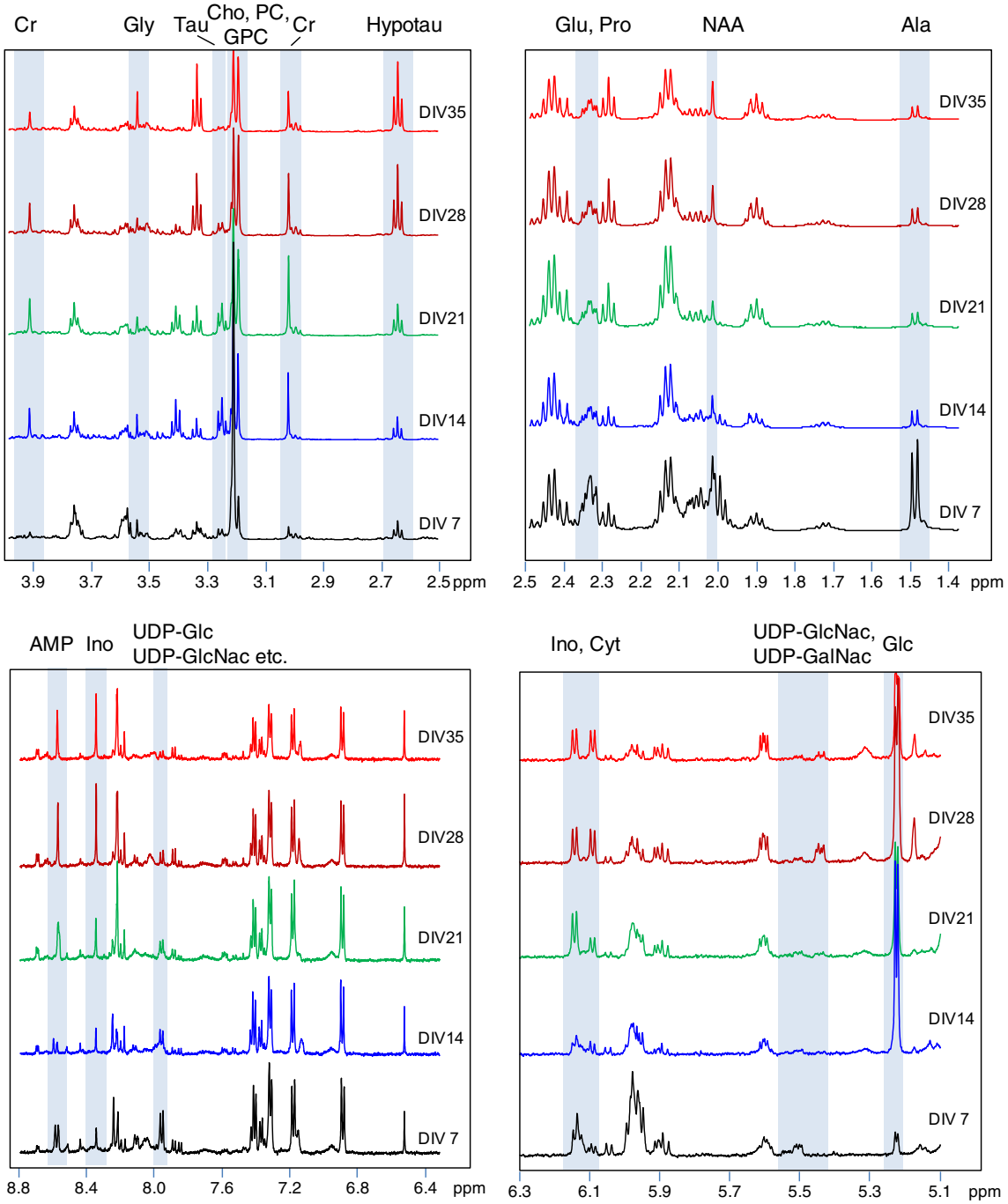

Fig. 2 Plot of mean spectra of 3D brain cell cultures collected at DIV 7, 14, 21, 28, and 35. **a** Spectral regions between 1.4 and 4 ppm are shown. **b** Spectral regions between 5.1 and 8.8 ppm are shown. Some prominent peak modifications are highlighted

Table 2 Coefficients of variation within (CVw) and between (CVb) the different brain batches obtained at the five different time points (DIV 7, DIV 14, DIV 21, DIV 28, DIV 35) as well as the mean over the different time points

	DIV 7	DIV 14	DIV 21	DIV 28	DIV 35	Mean
CVw	8.2%	5.1%	6.2%	9.0%	9.2%	7.6%
CVb	12.2%	7.8%	10.0%	10.4%	9.6%	10.0%

analyses were repeated employing all buckets from spectra of the brain aggregates (Fig. 4). The different developmental steps were completely separated in both PCA and oPLS ($Q^2 = 0.99$, Permutation test: $p < 0.001$). The better separation compared to the analysis of the assigned metabolites only is probably due to the higher number of included variables and the relatively reduced impact of low intensity metabolites. However, the loading plot (Fig. 4c) revealed the same discriminating metabolites (especially PC, Hypotau, Tau, Cho, Cre).

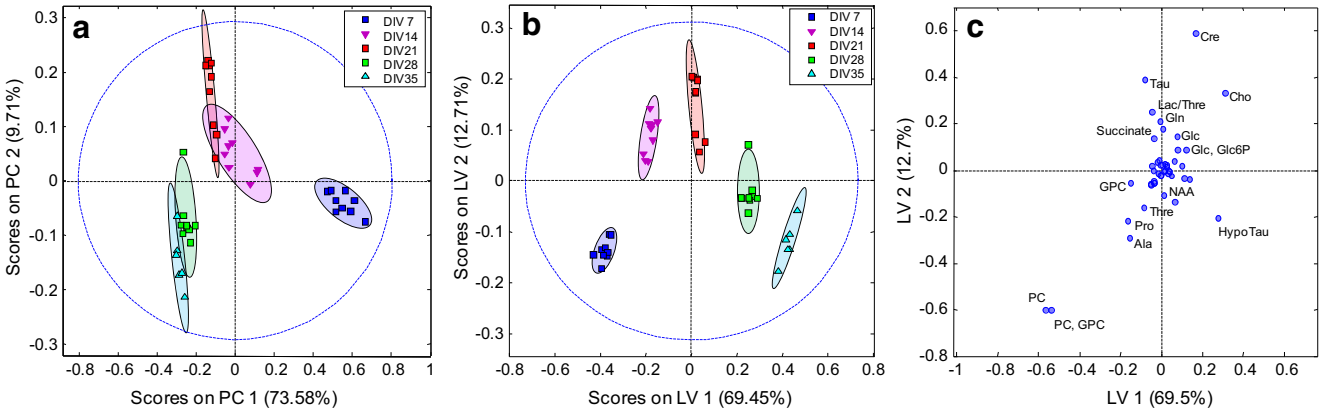

Fig. 3 Scores plot of a PCA analysis (**a**) and an oPLS analysis (**b**) employing only assigned metabolites from spectra of 3D brain cell cultures measured at five different developmental stages (DIV 7, 14, 21, 28, 35). The different maturation stages are separated. In general, metabolic changes appear stronger in the earlier phases of the culture. The ellipsoids correspond to confidence intervals at an 84% level. **c** PLS loading plot with the main discriminating metabolites labeled

The same chemometric analyses were performed on the cell media supernatants to determine temporal changes in uptake of cell media substances and of metabolic release into the supernatant. Again, the analyses were performed on assigned metabolites only and on all buckets. The results are shown in the ESM, Figs. S1 and S2. Also for cell media, a clear separation of the developmental steps was determined in PCA and oPLS, primarily for the early stages, DIV 7 and DIV 14, while later stages demonstrate partly overlapping confidence intervals (ESM Figs. S1a, b and S2a, b), indicating lesser changes of metabolite uptake and release after DIV 21. The corresponding loading plots (ESM Figs. S1c and S2c) reveal as main discriminating metabolites (with strongest absolute changes) lactate (Lac), which increased over time (indicating higher release into the medium), glutamine (Gln), which was low early on and increased soon after (indicating higher release), glucose (Glc), which decreased over time (indicating increasing cell uptake), or isoleucine (Ile), leucine (Leu), and valine (Val), which were high early on, then decreased (indicating increasing uptake), followed by a slight increase. As for the cell aggregates, additional other metabolites of lower concentration also show comparable relative changes.

In order to check the metabolite content variability between the four different measured brain batches, the chemometric analysis was repeated with the brain batches as discriminant in a PLS-DA (discriminant analysis) (results not shown). No separation between the different cell batches was found in this discriminant analysis. This result together with the tight clustering shown in Fig. 4 suggests that the metabolite profiles are well reproducible within and between the different brain batches. Similarly, the calculation of the coefficients of variation within and between the brain batches corroborated this result (see above).

Correlation analysis

Correlations between the temporal changes of assigned metabolites were probed in order to investigate potential

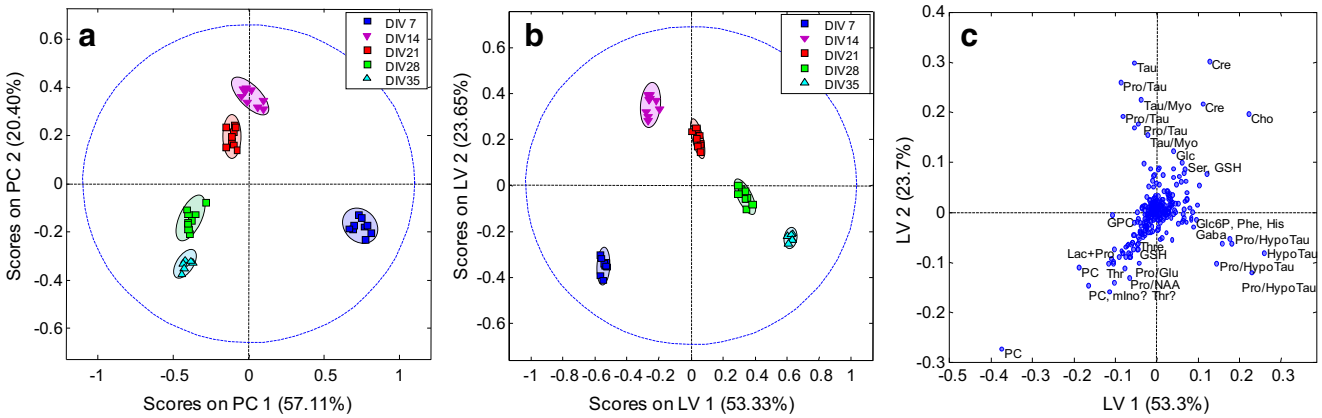

Fig. 4 Scores plot of a PCA analysis (**a**) and an oPLS analysis (**b**) employing all resonances (buckets) from spectra of 3D brain cell cultures measured at five different developmental stages (DIV 7, 14, 21, 28, 35). The different maturation stages are entirely separated. In general, metabolic changes appear stronger in the earlier phases of the culture maturation. **c** PLS loading plot with the main discriminating metabolites labeled

common biochemical pathways and for physiological interpretation of brain cell aggregate maturation. The metabolite correlation map is shown in Fig. 5, illustrating correlations on a heat-map. The assigned metabolites are grouped by similarity. Interestingly, numerous highly positive and negative correlations were obtained. The amino acids alanine (Ala), Pro, threonine (Thr), Ile, Val, and Leu correlate highly positively, while they are rather not or negatively correlated to glycine (Gly) or serine (Ser). Glutathione (GSH), PC, and GPC also correlate strongly and positively with Ala, Pro, Thr, Ile, Val, and Leu and on the other hand negatively with myo-inositol (mIno), Cho, Cre, and Glc. The temporal evolution of Tau correlates solely and negatively with NAA, which corresponds to the recent finding of developmental replacement of Tau by NAA [49]. However, besides indicating potential physiological relations between metabolite changes, the correlations may as well be coincidental.

A correlation map with variable reordering was also calculated for the assigned metabolites of the cell media supernatants (ESM Fig. S3). Strong positive and negative correlations were detected as well, e.g., the amino acids Thr, Lys, Phe, tyrosine (Tyr), arginine (Arg), Ser, histidine (His), and tryptophan (Trp) all correlate positively with

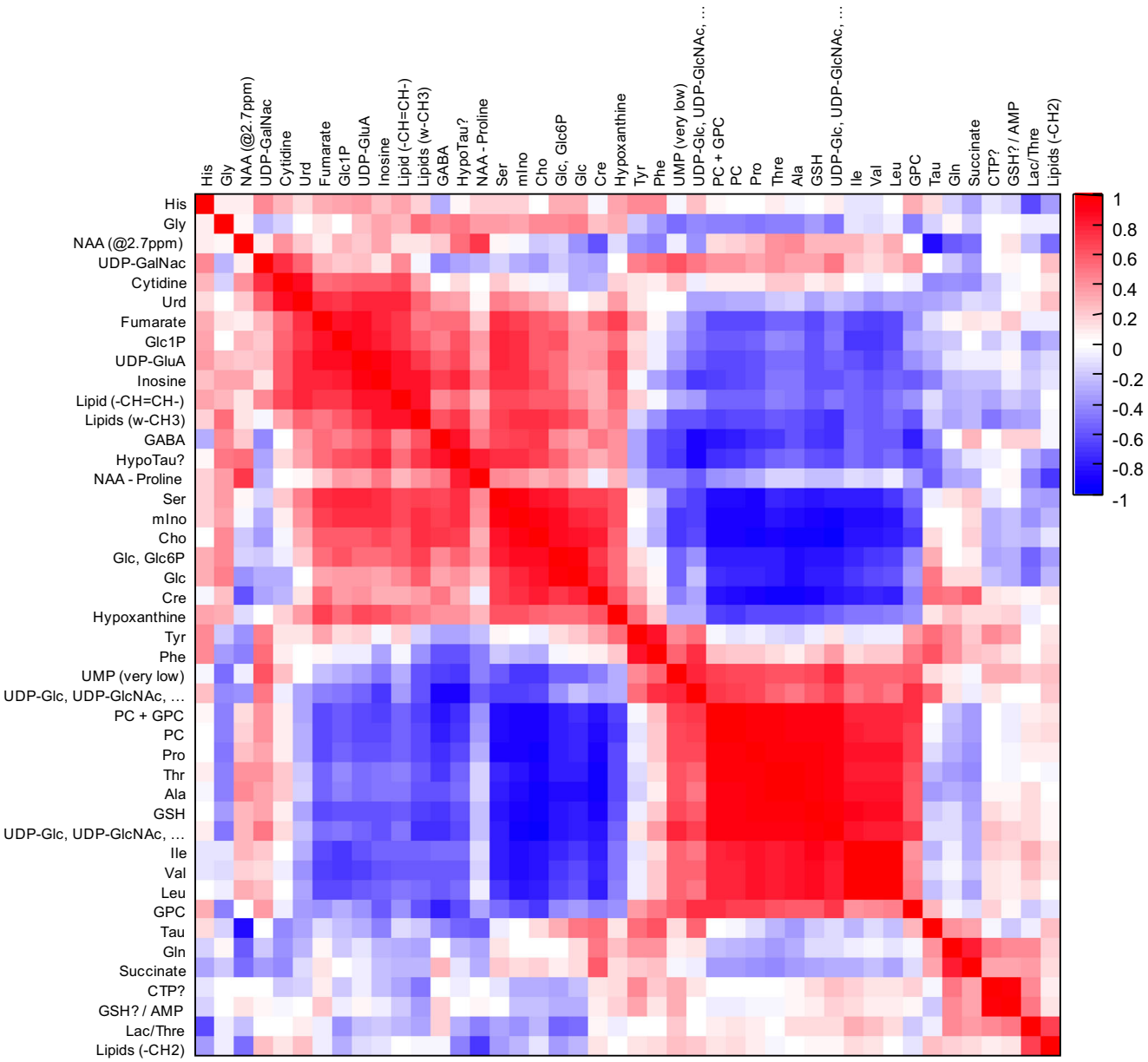

Fig. 5 Metabolite correlation map (taking all DIVs into account) grouped by similarity among each assigned metabolite from cell aggregates. Correlation degrees are shown using a color scale from blue (negative correlation) to red (positive correlation), allowing elucidation of inter-metabolite correlations

each other, but not with Leu, Val, and Ile, which themselves correlate positively. Ala does not correlate positively with any other assigned amino acid.

Evolution of individual metabolites during maturation

The analysis of individual metabolites over the developmental process revealed specific and variable time courses (Fig. 6). While some metabolites increased (e.g., GABA, Cho, Hypotau, mIno) or decreased over time (e.g., PC, Ala, Pro, GSH, Thr), some others were less affected (e.g., Val). Several metabolites showed a more complex evolution, such as Tau which decreased but only after a strong initial increase. For some metabolites (e.g., Ala, Pro, Tau, GSH, Cre), strong changes occurred primarily during the early maturation period. On the other hand, Hypotau increased strongly towards the end of the development but showed only little change during the early maturation process. Kinetic fitting was performed for most metabolites undergoing temporal changes to determine the most likely kinetic model and potential kinetic parameters.

The observed metabolic changes reflect the ongoing differentiation of the brain aggregates into the various cell phenotypes, i.e., neurons, astrocytes, oligodendrocytes, and microglial cells [37], as well as their maturation and are in line

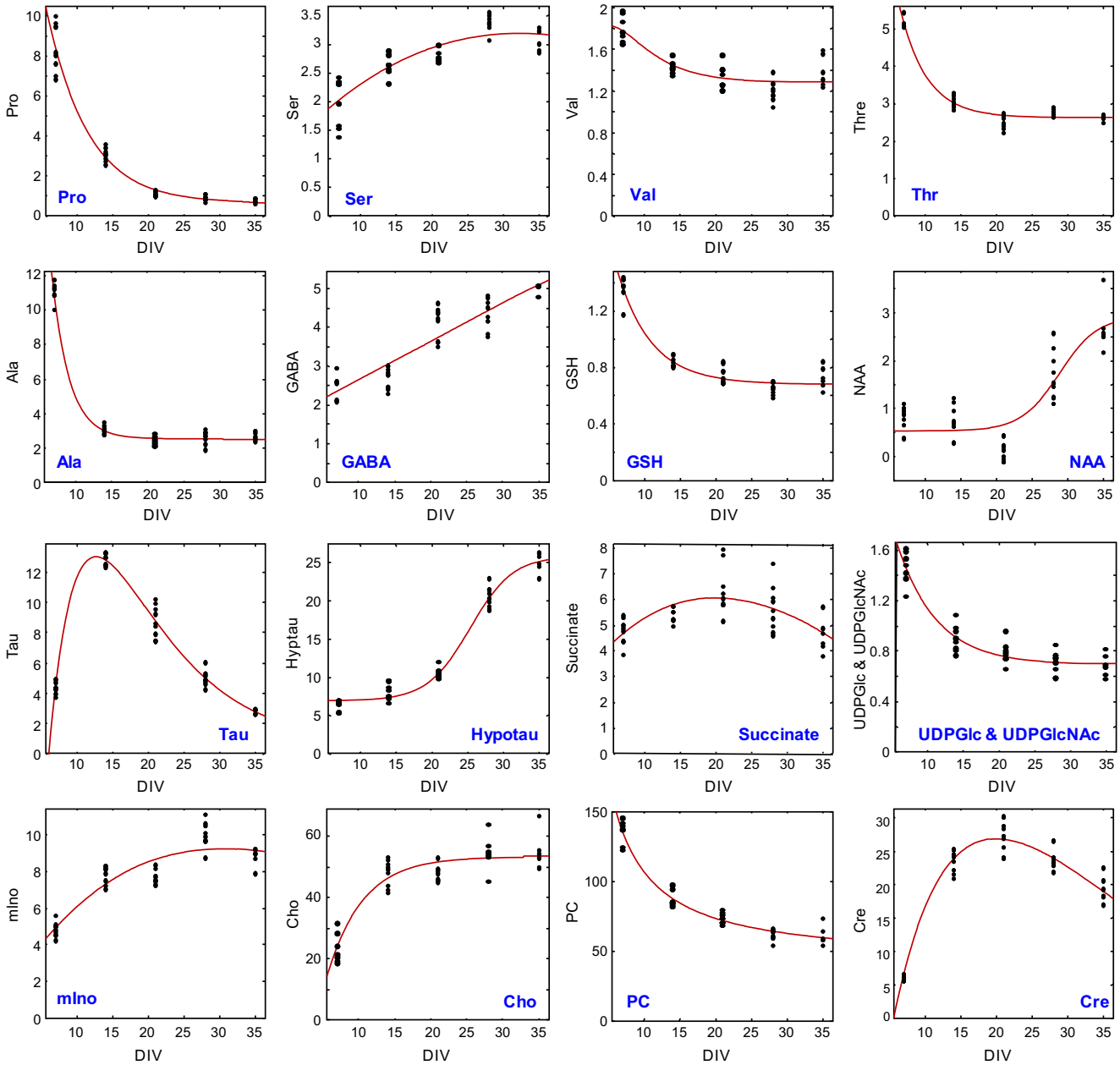

Fig. 6 Time evolution of selected metabolites over time in culture with fitting of the kinetic (solid line). The *x*-axis shows the days in vitro (DIV) and the *y*-axis the metabolite content in arbitrary unit. Dots represent individual measurements

with our previous observations. The increase in GABA, an important neurotransmitter, and in choline, precursor of the neurotransmitter acetylcholine, is perfectly correlated with the maturation of neurons as observed by the increase in the mRNA and protein expression levels for neurofilaments, which are part of the neuronal cytoskeleton, and the increase in the activity of glutamic acid decarboxylase and acetylcholine esterase, enzymes specific for GABAergic and cholinergic neurons, respectively [9]. The observed decrease in glutathione content with cellular maturation was also confirmed in our model by spectrophotometric assay [50]. Furthermore, the peak of intracellular Tau concentration observed in this study coincides with the start of intense myelination in the brain aggregates [50] which is in line with the recent report on the oligodendrocyte-differentiation-enhancing activities of Tau [51].

The general direction of change during chick embryo brain maturation from incubation days 10 to 20 and postnatal day 1 for Tau, PC, Ala (decrease), mIno, GABA, Gly, Cho (increase), NAA (delayed increase), and Gln (only modest changes) [36] corresponds to the changes found in brain aggregates; however, not surprisingly, the kinetic time curves differ and appeared more complex in the brain aggregates, since the developmental window covered in our study is broader.

The evolution of individual metabolites in cell media supernatants was briefly described in the chemometric analysis above and is not presented in detail. Santos et al. [35] described reduced uptake of alanine and branched-chain amino acids from culture medium of rat brain cell aggregates during development, which does not match our finding indicating rather increasing uptake until DIV 21 and only thereafter a decrease. This may be due to the differences in cell culture media composition used in the two studies, as well as to the clear differences in the cell composition of the cultures, since Santos et al. report a higher proportion of astrocytes as compared to neurons than us at late developmental stage [9, 37].

Metabolic changes of the developing brain have also been investigated non-invasively by in vivo MR spectroscopy in animal models and also in humans [15–21]. In vivo NMR measurements commonly report clear NAA and Cre increases during brain development, which is in line with our findings in the 3D rat brain cell aggregates. In contrast, most in vivo NMR studies demonstrated mIno to decrease during maturation in human and animal models [15, 19, 20], which is opposite to our finding in cell aggregates where a rather constant level is observed after an initial increase (Fig. 6). However, mIno was found to increase during rat brain development in another study [21] in accordance with our results. A strong decrease was noted for taurine in the developing rat brain [16], in line with our finding of a strong decrease following a very early rise. Developmental differences between studies were attributed to differences in animal species or to regional differences in the brain [16].

Lipid analysis

Because of short relaxation times, lipids can generally best be determined from spectra acquired without a T_2 -filter. The methyl and especially the methylene resonances at 0.9 and

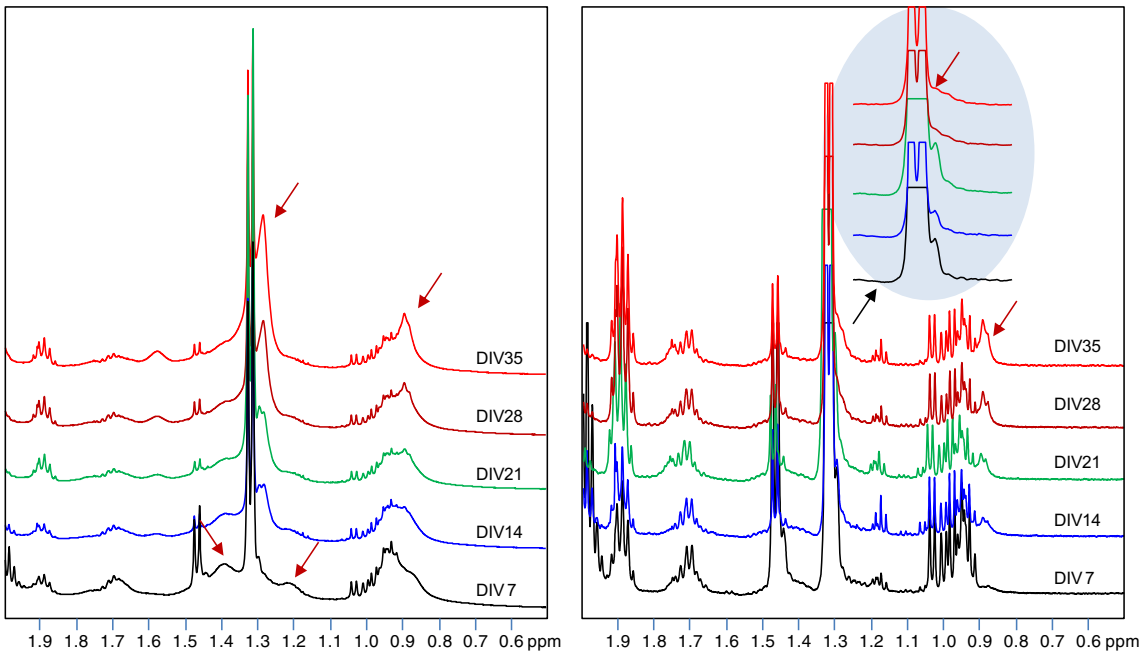

Fig. 7 Left: Plot of 1D NOESY spectra at the five different DIVs demonstrating the evolution of the lipid methyl and methylene resonances. Right: Plot of T_2-filtered PROJECT spectra at the five different DIVs demonstrating the evolution of the lipid methyl and methylene resonances. The insert zooms into the 1.1–1.3-ppm region to demonstrate the decay of a narrow methylene resonance (probably due to more mobile lipids), while the broader methyl and methylene resonances increase during evolution

1.3 ppm, respectively, that arise from protons of fatty acyl chains demonstrated visually an increase in the 1D NOESY spectra (Fig. 7 left). However, different lipid compartments appear to be visible in the HR-MAS spectra presenting with different linewidths. While the methylene resonance with a smaller linewidth increases strongly, a broader component, which is most likely due to a less mobile lipid compartment, appears to decrease (Fig. 7 left). Another (third) lipid compartment becomes visible in the PROJECT spectra only at long echo times (Fig. 7 right). While the (broader) methyl resonance increases during the development, another methylene resonance with small linewidth clearly decreases during development (zoomed in region in Fig. 7 right). This lipid compartment probably arises from fatty acids or from lipid droplets, which are relatively mobile and become therefore visible at long echo times. However, a detailed lipid analysis is beyond the scope of this paper. The lipid visibility depends strongly on measurement parameters like echo time or spinning rate of the HR-MAS measurement [52] and a detailed analysis would require additional investigations, e.g., changing the spinning speed and determination of intermolecular cross-relaxation rates, which would then allow to study membrane binding, organization, localization, and orientation of membrane-embedded molecules [53–55].

The most prominent resonances of the 1D NOESY spectra arising from different lipid moieties were investigated for relative changes during maturation. In Fig. 8, the developmental changes are shown for the ratio of the alkene protons from unsaturated lipids (-CH=CH-) at 5.32 ppm over the methyl and the methylene peaks (Fig. 8 a, b) and for the methylene- over methyl-ratio (Fig. 8c). The plots demonstrate a stronger increase of the unsaturated lipid resonance (-CH=CH-) compared to the methylene and methyl moieties and a stronger increase of the methylene than the methyl resonance. These results indicate an increasing unsaturation grade of the lipids, as well as an elongation of the lipid chain length during AGGR maturation, in line with the ability of fetal rat brain to elongate and desaturate fatty acids [56] and with the increase in chain length and greater unsaturation proportion reported in vivo and in vitro during maturation [57, 58].

Conclusion

Time-dependent changes in intracellular metabolite concentration of aggregating brain cell cultures could be followed by ^{1}H HR-MAS NMR. This high content OMICS technique revealed strong and various metabolic alterations during the brain aggregate development which emphasizes the complexity of this culture system and most likely reflects the physiological processes occurring during brain development. Only small variations between biological replicates of the same development point were observed, but a very clear separation of the metabolites among the different time points of cell collection was revealed by PCA, oPLS, and individual metabolite analyses, proving the robustness of ^{1}H HR-MAS NMR applied to 3D brain cell cultures.

The obtained metabolic fingerprint of 3D brain cell cultures at different maturation stages is an important knowledge that will refine the selection of the best windows of vulnerability for toxicological investigations, as well as for investigating neurological disorders and the effects of brain infections, including Zika virus infection, on brain cell metabolism. HR-MAS NMR has the advantage of establishing the metabolome in intact cells and will most likely contribute to improve predictive neurotoxicology, in the context of drug safety assessment and for the evaluation of the impact of environmental chemicals on human health, by providing detailed mechanistic information of altered cellular processes. We hypothesize that

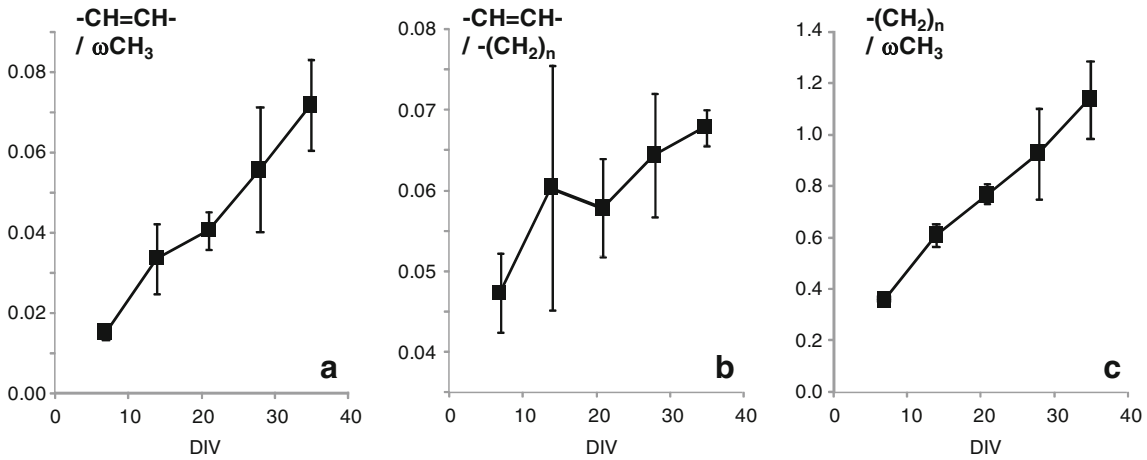

Fig. 8 Lipid peak intensity ratio as function of the DIV. Squares represent the averaged ratios of the nine measurements per DIV (respectively six measurements at DIV 35). Error bars represent standard deviations. **a** Ratio of unsaturated lipid (-CH=CH-) over methyl (ω-CH_3). **b** Ratio of the unsaturated lipid (-CH=CH-) over methylene (-CH_2)$_n$. **c** Ratio of methylene (-CH_2)$_n$ over methyl (ω-CH_3)

metabolic profiling by HR-MAS NMR will yield biomarkers that are indicative for toxicological processes.

Acknowledgements This work was supported by the UniBE ID-Grant (PV), Swiss National Science Foundation SNF grant no. 200021_14438 (MV), and Swiss Centre for Applied Human Toxicology (SCAHT) grant (MGZ).

Compliance with ethical standards

Conflict of interest The authors declare that they have no conflict of interest.

Ethical approval Ethical approval was obtained from the VD Service de la consommation et des affaires vétérinaires (authorization number VD3128). Animals were housed and handled following the guidelines of the Ethics Committee for Animal Experimentation of the Swiss Academy of Medical Sciences (SAMS) and the Swiss Academy of Sciences (SCNAT).

References

1. Grandjean P, Landrigan PJ. Developmental neurotoxicity of industrial chemicals. Lancet. 2006;368(9553):2167–78.
2. Kola I, Landis J. Can the pharmaceutical industry reduce attrition rates? Nat Rev Drug Discov. 2004;3(8):711–5.
3. Man F, Anna T, Kathy M, Wu JH, Ken H, Edmundo M. Evaluation of the characteristics of safety withdrawal of prescription drugs from worldwide pharmaceutical markets—1960 to 1999. Drug Inf J. 2001;35(1):293–317.
4. Coecke S, Eskes C, Gartlon J, Kinsner A, Price A, van Vliet E, et al. The value of alternative testing for neurotoxicity in the context of regulatory needs. Environ Toxicol Pharmacol. 2006;21(2):153–67.
5. Bal-Price AK, Hogberg HT, Buzanska L, Coecke S. Relevance of in vitro neurotoxicity testing for regulatory requirements: challenges to be considered. Neurotoxicol Teratol. 2010;32(1):36–41.
6. OECD. Test no. 424: neurotoxicity study in rodents, OECD guidelines for the testing of chemicals, section 4, no. 424, OECD Publishing, Paris. 1997. https://doi.org/10.1787/9789264071025-en. Accessed 27 April 2018.
7. OECD. Test no. 426: developmental neurotoxicity study, OECD guidelines for the testing of chemicals, section 4, no. 426, OECD Publishing, Paris. 2007. https://doi.org/10.1787/9789264067394-en. Accessed 27 April 2018.
8. Crofton KM, Mundy WR, Lein PJ, Bal-Price A, Coecke S, Seiler AE, et al. Developmental neurotoxicity testing: recommendations for developing alternative methods for the screening and prioritization of chemicals. ALTEX. 2011;28(1):9–15.
9. Honegger P, Defaux A, Monnet-Tschudi F, Zurich MG. Preparation, maintenance, and use of serum-free aggregating brain cell cultures. Methods Mol Biol. 2011;758:81–97.
10. Schultz L, Zurich MG, Culot M, da CA LC, Bellwon P, et al. Evaluation of drug-induced neurotoxicity based on metabolomics, proteomics and electrical activity measurements in complementary CNS in vitro models. Toxicol In Vitro. 2015;30(1 Pt A):138–65.
11. Prieto P, Kinsner-Ovaskainen A, Stanzel S, Albella B, Artursson P, Campillo N, et al. The value of selected in vitro and in silico methods to predict acute oral toxicity in a regulatory context: results from the European Project ACuteTox. Toxicol in Vitro. 2013;27(4):1357–76.
12. Zurich MG, Stanzel S, Kopp-Schneider A, Prieto P, Honegger P. Evaluation of aggregating brain cell cultures for the detection of acute organ-specific toxicity. Toxicol in Vitro. 2013;27(4):1416–24.
13. Zurich MG, Eskes C, Honegger P, Berode M, Monnet-Tschudi F. Maturation-dependent neurotoxicity of lead acetate in vitro: implication of glial reactions. J Neurosci Res. 2002;70(1):108–16.
14. Smirnova L, Hartung T. Chapter 14—human 3D in vitro models for developmental neurotoxicity. In: Paule MG, Wang C, editors. Handbook of developmental neurotoxicology (Second Edition). Academic Press; 2018. p. 163–72.
15. Kreis R, Hofmann L, Kuhlmann B, Boesch C, Bossi E, Hüppi PS. Brain metabolite composition during early human brain development as measured by quantitative in vivo 1H magnetic resonance spectroscopy. Magn Reson Med. 2002;48:949–58.
16. Ramu J, Konak T, Liachenko S. Magnetic resonance spectroscopic analysis of neurometabolite changes in the developing rat brain at 7T. Brain Res. 2016;1651:114–20.
17. Kato T, Nishina M, Matsushita K, Hori E, Mito T, Takashima S. Neuronal maturation and N-acetyl-L-aspartic acid development in human fetal and child brains. Brain Dev. 1997;19(2):131–3.
18. Xu D, Bonifacio SL, Charlton NN, Vaughan P, Lu Y, Ferriero DM, et al. MR spectroscopy of normative premature newborns. J Magn Reson Imaging. 2011;33(2):306–11.
19. Card D, Nossin-Manor R, Moore AM, Raybaud C, Sled JG, Taylor MJ. Brain metabolite concentrations are associated with illness severity scores and white matter abnormalities in very preterm infants. Pediatr Res. 2013;74(1):75–81.
20. Tanifuji S, Akasaka M, Kamei A, Araya N, Asami M, Matsumoto A, et al. Temporal brain metabolite changes in preterm infants with normal development. Brain Dev. 2017;39(3):196–202.
21. Tkac I, Rao R, Georgieff MK, Gruetter R. Developmental and regional changes in the neurochemical profile of the rat brain determined by in vivo 1H NMR spectroscopy. Magn Reson Med. 2003;50(1):24–32.
22. Clarke CJ, Haselden JN. Metabolic profiling as a tool for understanding mechanisms of toxicity. Toxicol Pathol. 2008;36(1):140–7.
23. Leenders J, Frederich M, de Tullio P. Nuclear magnetic resonance: a key metabolomics platform in the drug discovery process. Drug Discov Today Technol. 2015;13:39–46.
24. Power WP. High-resolution magic angle spinning-enabling applications of NMR spectroscopy to semi-solid phases. Annu Rep NMR Spectrosc. 2011;72:111–56.
25. Vermathen M, Paul LEH, Diserens G, Vermathen P, Furrer J. 1H HR-MAS NMR based metabolic profiling of cells in response to treatment with a hexacationic ruthenium metallaprism as potential anticancer drug. PLoS One. 2015;10(5):e0128478.
26. Griffin JL, Shockcor JP. Metabolic profiles of cancer cells. Nat Rev Cancer. 2004;4(7):551–61.
27. Moestue S, Sitter B, Bathen TF, Tessem MB, Gribbestad IS. HR MAS MR spectroscopy in metabolic characterization of cancer. Curr Top Med Chem. 2011;11(1):2–26.
28. Smith SJ, Wilson M, Ward JH, Rahman CV, Peet AC, Macarthur DC, et al. Recapitulation of tumor heterogeneity and molecular signatures in a 3D brain cancer model with decreased sensitivity to histone deacetylase inhibition. PLoS One. 2012;7(12):e52335.
29. Keshari KR, Sriram R, Van CM, Wilson DM, Wang ZJ, Vigneron DB, et al. Metabolic reprogramming and validation of hyperpolarized 13C lactate as a prostate cancer biomarker using a human prostate tissue slice culture bioreactor. Prostate. 2013;73(11):1171–81.
30. Bollard ME, Xu J, Purcell W, Griffin JL, Quirk C, Holmes E, et al. Metabolic profiling of the effects of D-galactosamine in liver spheroids using (1)H NMR and MAS-NMR spectroscopy. Chem Res Toxicol. 2002;15(11):1351–9.
31. Rosi A, Grande S, Luciani AM, Barone P, Mlynarik V, Viti V, et al. (1H) MRS studies of signals from mobile lipids and from lipid

metabolites: comparison of the behavior in cultured tumor cells and in spheroids. NMR Biomed. 2004;17(2):76–91.
32. Sriram R, Van CM, Hansen A, Wang ZJ, Vigneron DB, Wilson DM, et al. Real-time measurement of hyperpolarized lactate production and efflux as a biomarker of tumor aggressiveness in an MR compatible 3D cell culture bioreactor. NMR Biomed. 2015;28(9):1141–9.
33. Esteve V, Berganzo J, Monge R, Martinez-Bisbal MC, Villa R, Celda B, et al. Development of a three-dimensional cell culture system based on microfluidics for nuclear magnetic resonance and optical monitoring. Biomicrofluidics. 2014 Nov;8(6):064105.
34. Duarte IF, Lamego I, Rocha C, Gil AM. NMR metabonomics for mammalian cell metabolism studies. Bioanalysis. 2009;1(9):1597–614.
35. Santos SS, Leite SB, Sonnewald U, Carrondo MJT, Alves PM. Stirred vessel cultures of rat brain cells aggregates: characterization of major metabolic pathways and cell population dynamics. J Neurosci Res. 2007;85(15):3386–97.
36. Feng Y, Zhu H, Zhang X, Wang X, Xu F, Tang H, et al. NMR based cerebrum metabonomic analysis reveals simultaneous interconnected changes during chick embryo incubation. PLoS One. 2015;10(10):e0139948.
37. Zurich MG, Monnet-Tschudi F, Costa LG, Schilter BT, Honegger P. Aggregating brain cell cultures for neurotoxicological studies. In vitro neurotoxicology. Springer; 2004. p. 243-66.
38. Aguilar JA, Nilsson M, Bodenhausen G, Morris GA. Spin echo NMR spectra without J modulation. Chem Commun. 2012;48(6):811–3.
39. Dieterle F, Ross A, Schlotterbeck G, Senn H. Probabilistic quotient normalization as robust method to account for dilution of complex biological mixtures. Application in 1H NMR metabonomics. Anal Chem. 2006;78(13):4281–90.
40. Wishart DS, Jewison T, Guo AC, Wilson M, Knox C, Liu Y, et al. HMDB 3.0—the human metabolome database in 2013. Nucleic Acids Res. 2013;41(Database issue):D801–7.
41. Govindaraju V, Young K, Maudsley AA. Proton NMR chemical shifts and coupling constants for brain metabolites. NMR Biomed. 2000;13:129–53.
42. Duarte JM, Lei H, Mlynarik V, Gruetter R. The neurochemical profile quantified by in vivo 1H NMR spectroscopy. Neuroimage. 2012 Jun;61(2):342–62.
43. Vermathen P, Capizzano AA, Maudsley AA. Administration and H-1 MRS detection of histidine in human brain: application to in vivo pH measurement. Magn Reson Med. 2000;43(5):665–75.
44. De Graaf RA, Chowdhury GM, Behar KL. Quantification of high-resolution (1)H NMR spectra from rat brain extracts. Anal Chem. 2011;83(1):216–24.
45. Yang Y, Chen L, Gao H, Zeng D, Yue Y, Liu M, et al. High-resolution magic-angle spinning (13)C spectroscopy of brain tissue at natural abundance. Magn Reson Chem. 2006 Mar;44(3):263–8.
46. Schurr PE, Thompson HT, Henderson LM, Williams JN Jr, Elvehjem CA. The determination of free amino acids in rat tissues. J Biol Chem. 1950;182:39–45.
47. Brand A, Leibfritz D, Hamprecht B, Dringen R. Metabolism of cysteine in astroglial cells: synthesis of hypotaurine and taurine. J Neurochem. 1998;71(2):827–32.
48. Sturman JA. Taurine in development. Physiol Rev. 1993;73(1): 119–47.
49. Nakada T. Conversion of brain cytosol profile from fetal to adult type during the perinatal period: taurine-NAA exchange. Proc Jpn Acad Ser B Phys Biol Sci. 2010;86(6):630–42.
50. Sandstrom J, Broyer A, Zoia D, Schilt C, Greggio C, Fournier M, et al. Potential mechanisms of development-dependent adverse effects of the herbicide paraquat in 3D rat brain cell cultures. Neurotoxicology. 2017;60:116–24.
51. Beyer BA, Fang M, Sadrian B, Montenegro-Burke JR, Plaisted WC, Kok BPC, et al. Metabolomics-based discovery of a metabolite that enhances oligodendrocyte maturation. Nat Chem Biol. 2018;14(1):22–8.
52. Precht C, Diserens G, Oevermann A, Vermathen M, Lang J, Boesch C, et al. Visibility of lipid resonances in HR-MAS spectra of brain biopsies subject to spinning rate variation. Biochim Biophys Acta. 2015;1851(12):1539–44.
53. Huster D, Arnold K, Gawrisch K. Investigation of lipid organization in biological membranes by two-dimensional nuclear overhauser enhancement spectroscopy. J Phys Chem B. 1999;103(1):243–51.
54. Scheidt HA, Huster D. The interaction of small molecules with phospholipid membranes studied by 1H NOESY NMR under magic-angle spinning. Acta Pharmacol Sin. 2008;29(1):35–49.
55. Scheidt HA, Pampel A, Nissler L, Gebhardt R, Huster D. Investigation of the membrane localization and distribution of flavonoids by high-resolution magic angle spinning NMR spectroscopy. Biochim Biophys Acta. 2004;1663(1–2):97–107.
56. Green P, Yavin E. Elongation, desaturation, and esterification of essential fatty acids by fetal rat brain in vivo. J Lipid Res. 1993;34(12):2099–107.
57. Van Aerde JE, Wilke MS, Feldman M, Clandinin MT. Accretion of lipid in the fetus and newborn. In: Polin RA, Fox WW, Abman SH, editors. Fetal and neonatal physiology. Third ed. Philadelphia: Elsevier, Saunders; 2004. p. 388–404.
58. Bourre JM, Honegger P, Daudu O, Matthieu JM. The lipid composition of rat brain aggregating cell cultures during development. Neurosci Lett. 1979;11(3):275–8.

Gaëlle Diserens PhD, is Postdoctoral Fellow in the methodological NMR group of the Department of BioMedical Research at the University of Bern. She is a bio-engineer and an experienced NMR spectroscopist.

Martina Vermathen PhD, is Senior Scientist and Research Assistant in the NMR group at the Department of Chemistry and Biochemistry at the University of Bern, Switzerland. As Principle Investigator, her research is focused on one hand of the NMR spectroscopic investigations of porphyrinic photosensitizers. On the other hand, her focus lies in HR-MAS NMR spectroscopic applications. She has worked in various projects and collaborations involving HR-MAS NMR, such as metabonomic studies of food stuff, cell cultures, and tissue samples.

Marie-Gabrielle Zurich biologist with a PhD in neurosciences, is Senior Scientist and Lecturer at the University of Lausanne, Switzerland, and for the Swiss Center for Applied Human Toxicology. She has strong experience in in vitro neurotoxicology. Her work focuses on the development of in vitro models for neurotoxicity testing, the search for biomarkers of neurotoxicity, and the metabolic changes occurring during glial reactivity.

Peter Vermathen is Associate Professor at the Departments of BioMedical Research and Radiology, at the University of Bern, Switzerland. He is a group leader in the Division of MR Methodology and Spectroscopy. The main thrust of his overall previous research has been in the area of in vivo MR spectroscopy. More recently, his focus expanded to include increasingly also ex vivo NMR with special emphasis on high-resolution magic angle spinning NMR of biopsies and cell cultures.